

CONFIRMATION OF A WARPED INNER DISK AROUND HD 100546

CATHERINE WALSH^{1,2} & CAIL DALEY³ & ATTILA? & STEFANO?

¹School of Physics and Astronomy, University of Leeds, Leeds, LS2 9JT, UK

²Leiden Observatory, Leiden University, P. O. Box 9531, 2300 RA Leiden, The Netherlands

³Astronomy Department, Wesleyan University, 96 Foss Hill Drive, Middletown, CT 06459, USA

ABSTRACT

Lorem ipsum dolor sit amet, consectetur adipiscing elit. Nullam condimentum pulvinar augue non finibus. Cras dignissim vel nunc a sollicitudin. Morbi sed mi at neque rhoncus cursus quis at nulla. Vestibulum ante ipsum primis in faucibus orci luctus et ultrices posuere cubilia Curae; Ut ut molestie felis. Etiam porta auctor magna, id consequat tortor. Cras rutrum metus eget porta vehicula. Ut diam orci, consectetur in lacinia eget, cursus vel ex. Nunc ut tellus sagittis, iaculis arcu non, feugiat lacus. Quisque sem turpis, pharetra sed ex nec, tempus pellentesque elit. Lorem ipsum dolor sit amet, consectetur adipiscing elit. Donec iaculis convallis mi, quis porttitor magna. In at finibus tellus, ut facilisis nulla. Aliquam fermentum tristique arcu, dignissim sagittis quam vulputate in.

1. INTRODUCTION

Observations of protoplanetary disks around nearby young stars offer unique insight into the initial conditions of planetary system formation. Resolved dust continuum observations from optical to cm wavelengths reveal the distribution of dust grains and can highlight signposts of ongoing planet formation and/or as yet unseen massive companions/planets, (e.g., cavities, gaps, rings, and spirals; see the recent reviews by [Espaillat et al. 2014](#), [Andrews 2015](#), and [Grady et al. 2015](#)).

As the second-most abundant gas-phase molecule in protoplanetary disks (after H₂), CO is a powerful diagnostic of various disk properties including gas mass (and surface density), kinematics, and gas temperature. The primary isotopologue, ¹²CO, is optically thick and thus emits from the warm disk atmosphere allowing derivation of the gas temperature in this region (e.g., [Williams & Cieza 2011](#); [Dutrey et al. 2014](#)). The rarer isotopologues (¹³CO, C¹⁸O, C¹⁷O and ¹³C¹⁸O) have progressively lower opacities and so enable penetration towards and into the disk midplane (see, e.g., recent theoretical studies by [Bruderer 2013](#), [Miotello et al. 2016](#), and [Yu et al. 2016](#)). In observations with sufficiently high spatial resolution, now routine with ALMA, this allows a direct determination of the location of the CO snowline with high precision (see, e.g., [Nomura et al. 2016](#); [Schwarz et al. 2016](#); [Zhang et al. 2017](#)). However, it has been demonstrated recently that chemistry, in particular isotope-selective photodissociation ([Visser et al. 2009](#)), can complicate the extraction of disk gas masses from CO isotopologue emission ([Miotello et al. 2014](#), [2016](#)).

Because emission from ¹²CO (and often ¹³CO) at (sub)mm wavelengths is bright, it has historically been used as a tracer of disk kinematics allowing a dynamical determination of the mass of the central star (e.g., [Simon et al. 2000](#)). However, gas motion can deviate from that expected solely due to Keplerian rotation because of various different physical effects, including the presence of spiral density waves, a substantial (and thus measurable) gas pressure gradient, radial flows mediated by accreting planets across cavities, or a disk warp, that can be revealed in spatially-resolved observations (see, e.g., [Rosenfeld et al. 2012](#); [Tang et al. 2012](#); [Casassus et al. 2013](#); [Rosenfeld et al. 2014](#); [Christiaens et al. 2014](#); [Casassus et al. 2015](#)). Spirals, radial flows, and warps are all signatures of the presence of (potentially massive) planetary companions; hence, perturbations from Keplerian motion traced in bright and spectrally- and spatially-resolved CO emission can expose unseen planets.

Here, we present high signal-to-noise and spectrally-resolved images of ¹²CO J = 3 – 2 emission from the protoplanetary disk around the nearby Herbig Ae star, HD 100546, observed during ALMA Cycle 0 operations. The HD 100546 disk has been proposed a host to (at least) two massive companions (see, e.g., [Acke & van den Ancker 2006](#); [Quanz et al. 2013](#); [Walsh et al. 2014](#)). In [Walsh et al. \(2014\)](#), henceforth referred to as Paper I, we presented the ¹²CO

($J = 3 - 2$) first moment map and dust continuum emission (at 302 and 346 GHz). These data spatially resolved the CO emission and allowed direct determination of the radial extent of the molecular disk (≈ 390 au, see also Pineda et al. 2014). The continuum data analysed in Paper I showed that the (sub)mm-sized dust grains had been sculpted into two rings. Pinilla et al. (2015) showed that this dust morphology is consistent with dust trapping by two massive companions: one with mass $\approx 20M_J$ at 10 au and one with mass $\approx 15M_J$ at 70 au. Emission from ^{12}CO ($J = 3 - 2$, 6 – 5, and 7 – 6) from HD 100546 had been detected previously with APEX (Panić et al. 2010). The APEX data also revealed an asymmetry in the red and blue peaks in the double-peaked line profiles most apparent in the $J = 3 - 2$ and 6 – 5 transitions. Panić et al. (2010) hypothesised that the asymmetry may arise due to shadowing of the outer disk by a warp in the inner disk.

Here, we revisit the HD 100546 ALMA Cycle 0 data by conducting a deeper analysis of the spatially and spectrally resolved ^{12}CO $J = 3 - 2$ emission. The focus of this work is the search for evidence of a warp in the inner regions of the disk as suggested in the single dish data presented in Panić et al. (2010). Using the same data set as here, Pineda et al. (2014) showed that the position-velocity (P-V) diagram across the major axis of the disk is better described by a disk inclination of $\approx 30^\circ$, rather than the 44° inclination which best reproduces the aspect ratio of the disk as seen in continuum emission (Paper I). In Section 2, we outline the imaging presented in the paper, in Section 3 we describe the modelling techniques used and present the results. Sections 4 and 5 discuss the implications and state the conclusions, respectively.

2. ALMA IMAGING OF HD 100546

HD 100546 was observed with ALMA on 2012 November 24 with 24 antennas in a compact configuration, with baselines ranging from 21 to 375 m. The self-calibrated and phase-corrected measurement set, produced as described in Paper I, is used in these analyses. In this work, we adopt the revised distance to HD 100546 determined by Gaia (109 ± 4 pc, Gaia Collaboration 2016a,b), and a stellar mass of $2.4M_\odot$, (van den Ancker et al. 1998)

In Paper I, the integrated intensity and first moment maps from the ^{12}CO $J = 3 - 2$ rotational transition at 345.795 GHz ($E_{\text{up}} = 33.19$ K and $A_{\text{ul}} = 2.497 \times 10^{-6} \text{ s}^{-1}$) were presented. The data cube from which those maps were produced was itself produced using the CASA task `clean` with Briggs weighting (robust=0.5) at a spectral resolution of 0.15 km s^{-1} . The resulting channel maps had an rms noise of $19 \text{ mJy beam}^{-1} \text{ channel}^{-1}$ and a synthesised beam of $0.^{\prime\prime}95 \times 0.^{\prime\prime}42$ (37°). The ^{12}CO was strongly detected with a signal-to-noise ratio (S/N) of 163 in the channel maps.

Because of the high S/N the imaging is redone here using uniform weighting which results in a smaller beam (and improved spatial resolution) at the expense of sensitivity. The resulting channel maps have an rms noise of $26 \text{ mJy beam}^{-1} \text{ channel}^{-1}$, a S/N of 106, and a synthesised beam of $0.^{\prime\prime}92 \times 0.^{\prime\prime}38$ (37°). Figure 1 presents the channel maps. Emission is detected ($\geq 3\sigma$) across 111 channels: the central channel is centred at the source velocity of 5.7 km s^{-1} as constrained previously by these data (see Paper I). The highest velocity emission detected is $\pm 8 \text{ km s}^{-1}$ relative to the source velocity. Given that the disk inclination (as constrained by the outer disk) is 44° and that the stellar mass is $2.4M_\odot$, emission is detected down to a radius of 15 au from the central star. Using the estimate of $\approx 30^\circ$ for the inclination of the inner disk from Pineda et al. (2014), reduces this radius to 8 au.

The channel maps in Figure 1 reveal the classic ‘butterfly’ morphology of spectrally- and spatially-resolved line emission from an inclined and rotating protoplanetary disk (see, e.g., Semenov et al. 2008). Compared with resolved ^{12}CO emission from other similarly inclined Herbig Ae disks at a similar spatial and spectral resolution (e.g., HD 163296, de Gregorio Monsalvo et al. 2013 and Rosenfeld et al. 2013, and HD 97048, Walsh et al. 2016 and van der Plas et al. (2017)), there is no evidence of emission from the back side of disk that is a signature of CO freezeout in the disk midplane coupled with emission from a flared surface. The blue-shifted emission also appears symmetric about the disk major axes indicating that the emission arises from a relatively ‘flat’ surface, in contrast with other Group I Herbig Ae/Be disks (e.g., HD 97048, Walsh et al. 2016; van der Plas et al. 2017). However, the emission is not wholly symmetric about the disk minor axis, with the red-shifted emission from the north-west quadrant appearing both fainter, and with a positional offset, relative to blue-shifted emission at the same velocity. In Figure 2 the channel maps from ± 0.45 to $\pm 1.5 \text{ km s}^{-1}$ are shown, now rotated clockwise to align the disk major axis in the vertical direction, and mirrored across the disk minor axis. Exhibiting the data in this velocity range and in this manner highlights the described asymmetry in brightness across the disk minor axis, the flatness of the emission, and the positional offset of the red-shifted north-west lobe relative to its blue-shifted counterpart.

Figure 3 present the moment maps (zeroth, first, second, and eighth). The zeroth moment map (integrated intensity) was produced using a 3σ rms noise clip. The line profile was extracted from a polygon delineated by the 3σ spatial extent of the emission in the channel maps. The first (intensity-weighted velocity), second (intensity-weighted velocity dispersion), and eighth (peak flux density) moment maps were produced using a more conservative clip of 6σ .

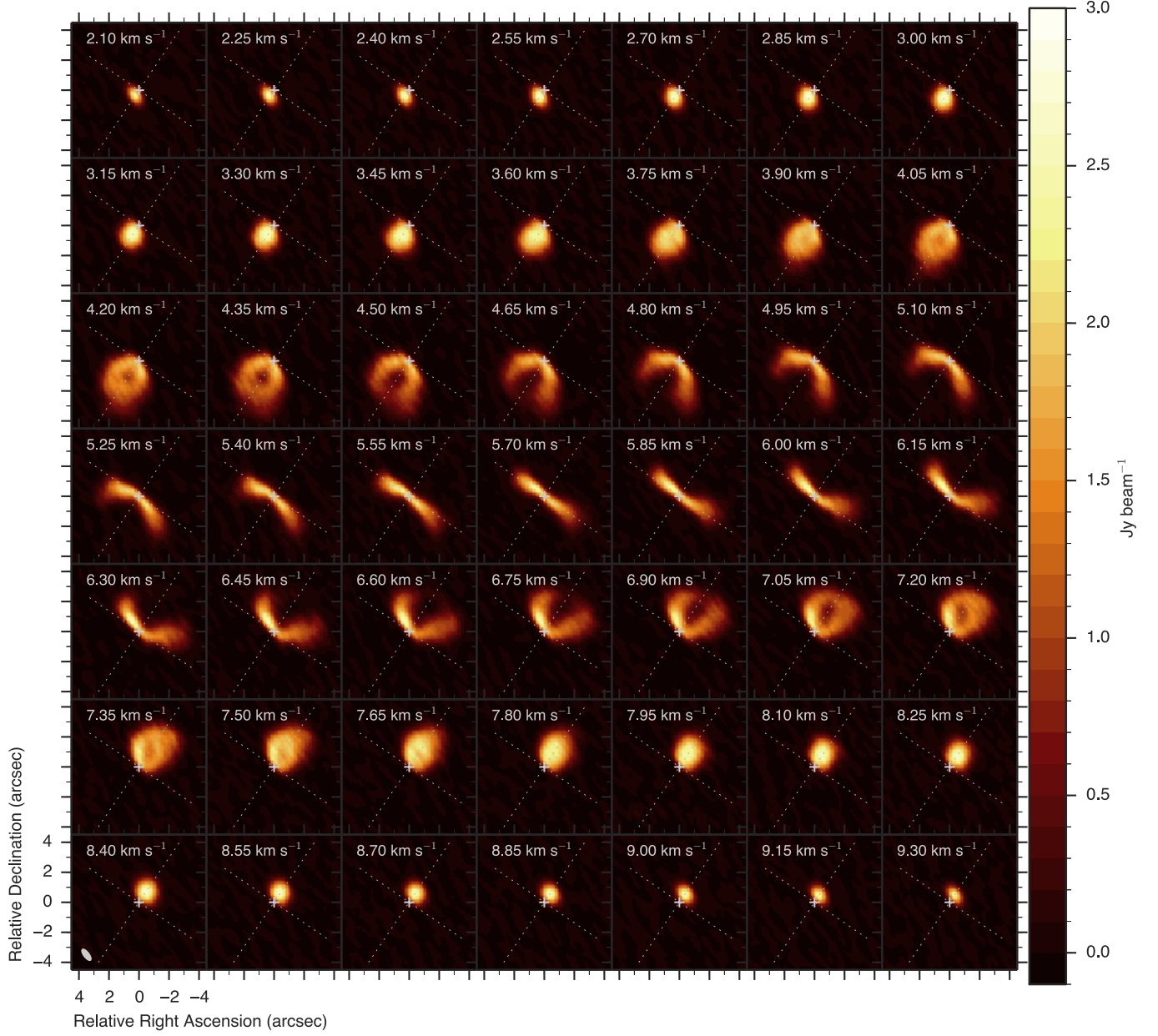


Figure 1. Channel maps of the CO $J = 3 - 2$ line emission imaged at a spectral resolution of 0.15 km s^{-1} . The dashed lines represent the disk major and minor axes determined from analysis of the continuum (Walsh et al. 2014).

The integrated intensity appears relatively symmetric about the disk minor axis; however, the ^{12}CO integrated emission extends further to the south-west than it does to the north-east. This asymmetry is also evident in the eighth-moment map with the north-east side of the disk appearing brighter than the south-west side. Both maps hint at emission from a flared disk which would lead to an asymmetry in emission across the disk major axis (i.e., the axis of inclination). The first and second moment maps also hint at asymmetric emission, in particular, the emission at the source velocity through the inner disk is twisted relative to the disk minor axis determined from the continuum emission. The velocity dispersion in the inner disk is also not wholly symmetric across the disk minor axis. Both images suggest the presence of a warp in the inner disk.

3. MODELLING THE KINEMATICS

Modelling of the kinematics as traced by the ^{12}CO emission is conducted using analytical models which describe the line-of-sight projected velocity, i.e. the first moment map. The model moment maps are convolved with the synthesised beam of the observations. The residuals (data – model) are in units of a single spectral resolution element

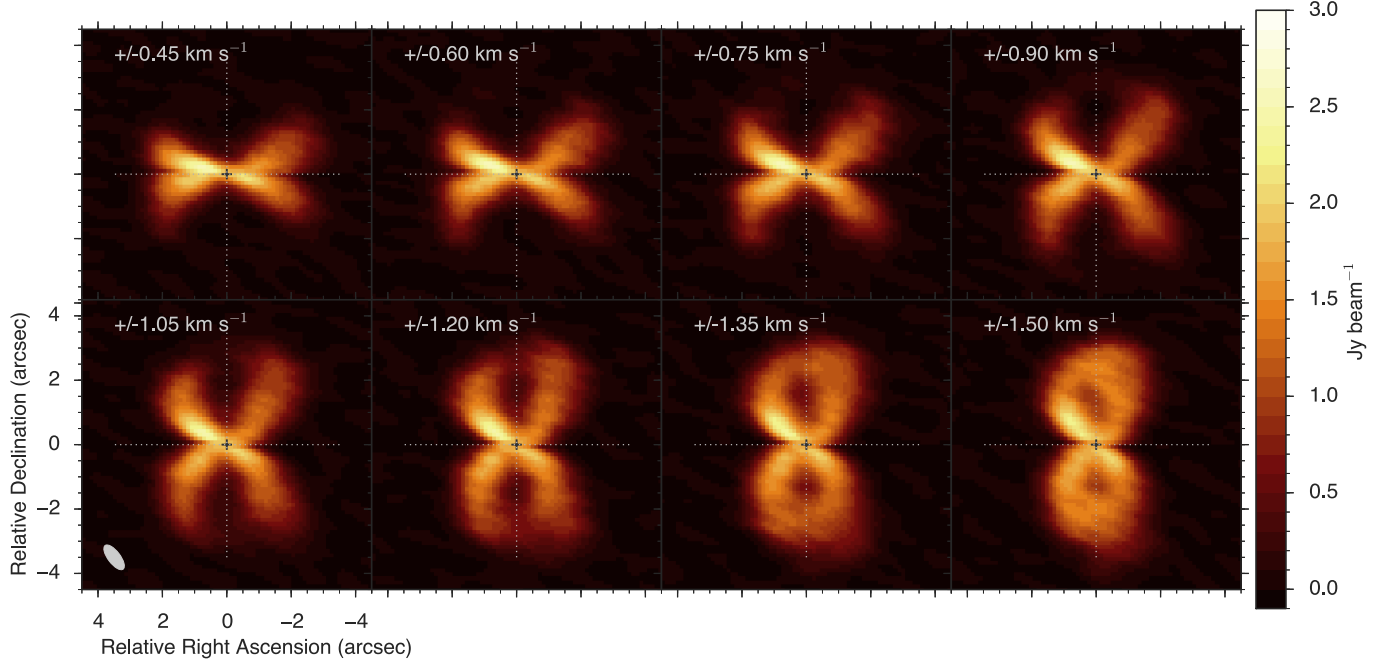


Figure 2. Channel maps of the CO $J = 3 - 2$ line emission rotated to align the disk major axis in the vertical direction, and mirrored across the disk minor axis.

($\delta v = 0.21 \text{ km s}^{-1}$). This discretisation is necessary because features smaller than the native spectral resolution of the data cannot be fit. We explore several metrics of ‘best fit’: (i) the total number of pixels for which the analytical and smoothed projected velocity reproduces the data within one spectral resolution element, (ii) the sum of the square of the residuals divided by the total number of pixels, and (iii) the magnitude of the peak residual. The total number of unmasked pixels in the observed first moment map is 2562.

Given the relatively small number of parameters for each model considered, the modelling approach is grid based, i.e. all possible grid combinations are explored.

3.1. A flat emitting surface

The simplest prescription for describing the first moment map of spectrally-resolved line emission from a disk is axisymmetric emission arising from a geometrically flat surface inclined to the line of sight. Assuming that the position angle of the disk is aligned with the y axis, the projected velocity on the sky relative to the observer is described by

$$v(x', y') = \sqrt{\frac{GM_*}{r}} \sin i \sin \theta, \quad (1)$$

where G is the gravitational constant, M_* is the mass of the central star, $r = \sqrt{x^2 + y^2}$ is the radius, i is the inclination, and $\theta = \arctan(y/x)$ (e.g., Rosenfeld et al. 2013). In this projection and for this particular orientation, $x = x'/\cos i$, $y = y'$, and $z = 0$. Model first moment maps for a flat disk with the same P.A. as HD 100546 at three different inclinations, 30° , 45° , and 60° , are shown in Figure A1 in the Appendix.

The wide range of disk inclinations ($[20^\circ, 60^\circ]$) and disk position angles ($[120^\circ, 170^\circ]$) explored are motivated by previous analyses of the continuum data which suggested a P.A. of $146^\circ \pm 4^\circ$ and an inclination of $44^\circ \pm 3^\circ$ (see Paper I and Pineda et al. 2014). Using the CO data, Pineda et al. (2014) suggest that the inner disk may be better described with an inclination of $\approx 30^\circ$ so we extend our explored range accordingly to ensure good coverage over the parameter space. First, a coarse grid with resolution 5° is run over the full parameter space, followed by a zoomed in region with resolution 1° .

The top-left panel of Figure 4 presents a 3D plot showing the total number of pixels which fit the data velocity field within one spectral resolution element, δv , as a function of disk inclination and position angle. The distribution is strongly peaked: the best-fit flat disk model using this metric has an inclination of 36° and a P.A. of 145° with 62.1% of model pixels lying within one spectral resolution element of the data. These data are also listed in Table 1. The P.A. is in excellent agreement with that derived from the continuum observations. The inclination, on the other hand,

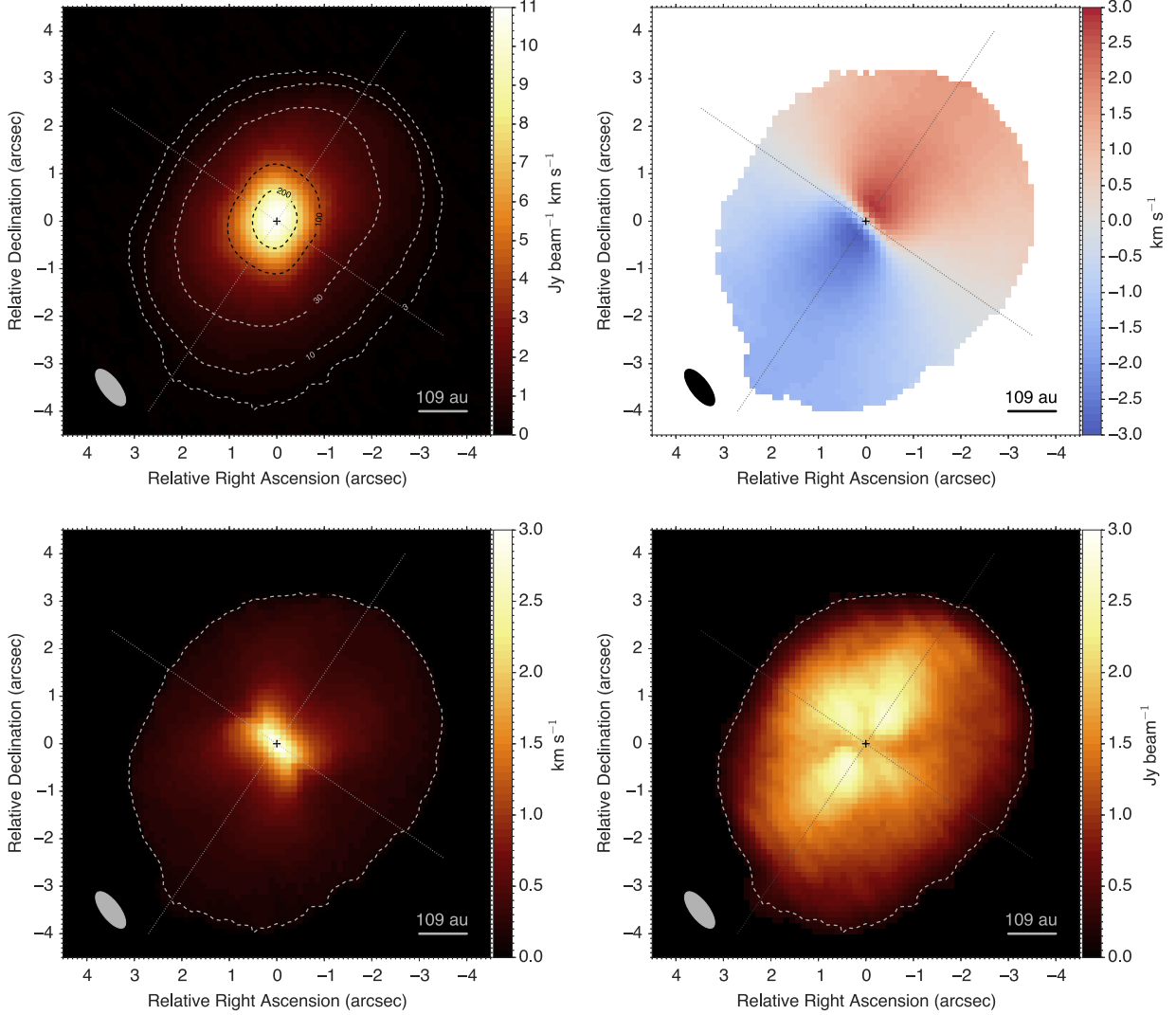


Figure 3. Moment maps for CO $J = 3 - 2$ line emission from HD 100546. Clockwise from top left: zeroth moment map (integrated intensity, Jy beam^{-1}), first moment map (intensity-weighted velocity, km s^{-1}), eighth moment map (peak intensity, Jy beam^{-1}), and second moment map (intensity-weighted velocity dispersion, km s^{-1}). The dashed contour in the second and eighth moment maps corresponds to the 3σ contour of the integrated intensity.

is lower and closer to the suggested inclination from Pineda et al. (2014).

The left hand plots of Figure 5 show the distribution of residuals summed over the entire disk (top panel) and the residual first moment map (bottom panel). The histogram of residuals shows small dispersion about 0 with 96.0% of pixels matching the data within $\pm 0.315 \text{ km s}^{-1}$). The residual map shows that a flat disk well reproduces the large-scale velocity field: the largest deviations from this model occur in the innermost disk where the model velocity field over-predicts the magnitude (by up to $7\delta v$) of the projected line-of-sight velocity along the minor axis of the disk. This leads to negative residuals in the north-east and positive residuals in the south-west. The morphology of the residuals suggests that the inner disk has an additional inclination along the minor axis of the outer disk, i.e., close to orthogonal to that of the outer disk.

3.2. A flared emitting surface

Although a geometrically flat disk well reproduces much of the the velocity field, particularly for the outer disk, we test next whether emission from a flared surface can improve upon the fit. This is important to check because HD 100546 is classified as a Group I (i.e., flared) Herbig Ae star (Meeus et al. 2001), so one might expect the ^{12}CO emission to arise from a layer higher up in the disk atmosphere. Indeed, thermo-chemical modelling of the disk around HD 100546 by Bruderer et al. (2012) suggests that the ^{12}CO line emission arises from a layer $z/r \approx 0.2$.

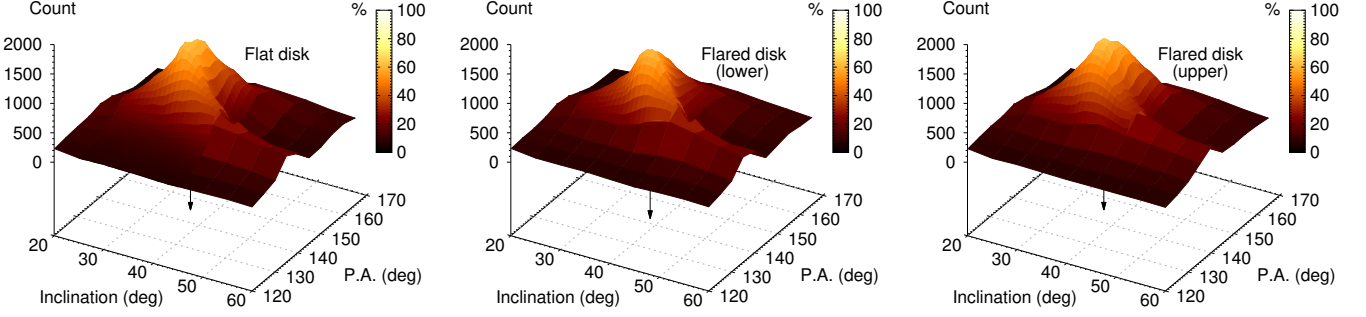


Figure 4. Distribution of model best-fit values using metric (i) as a function of inclination and position angle for the best-fit flat disk, flared disk (lower cone), and flared disk (upper cone), respectively. The best-fit opening angles, α , of the flared disks (with respect to the disk midplane) are 13° and 9° for the lower and upper cones, respectively. The percentage scale corresponds to the full range of pixel values (from 0 to 2652).

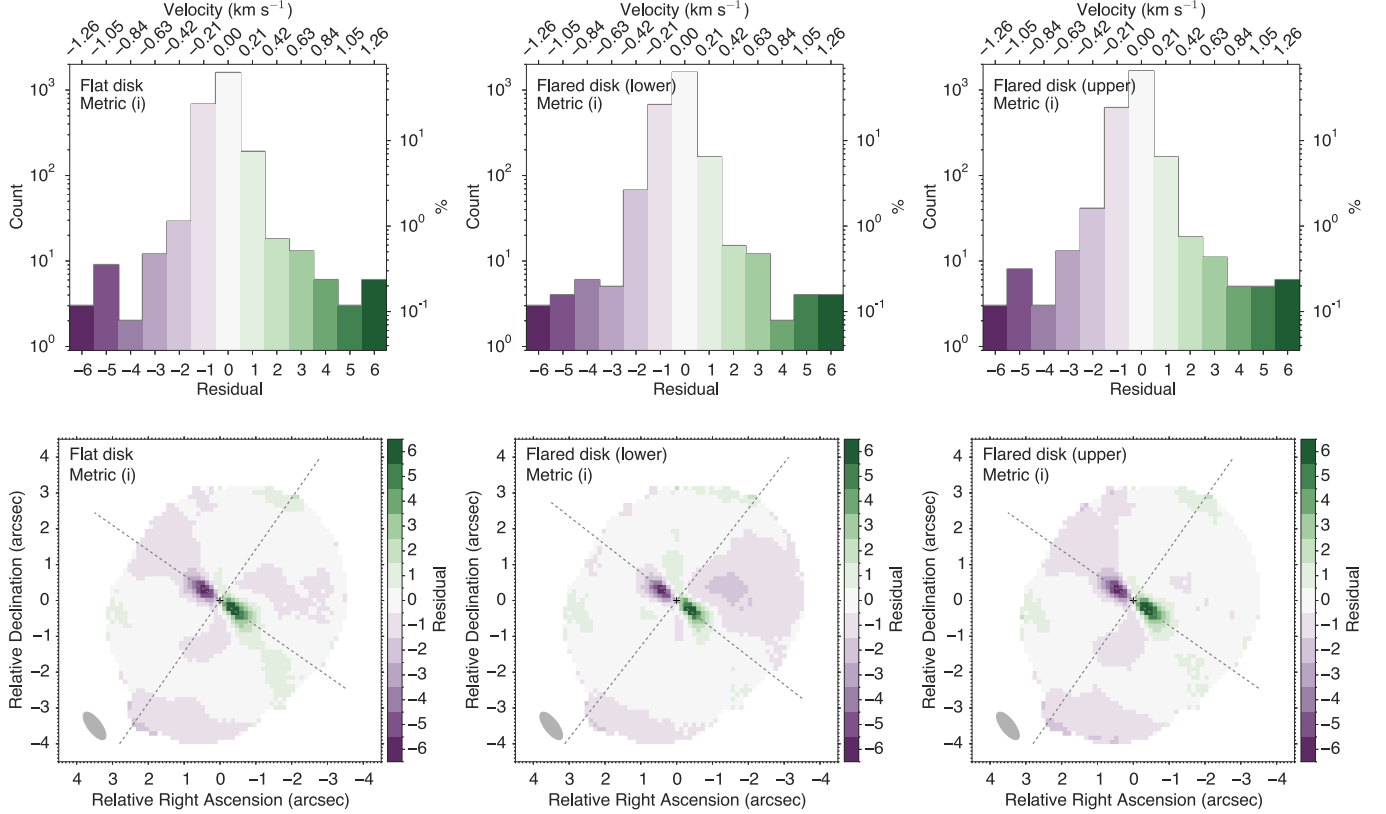


Figure 5. Residual histograms (top) and maps (bottom) using metric (i) as the measure of best fit for a geometrically flat disk (left), and the lower cone (middle) and upper cone (right) of a flared disk. The histograms are displayed on a log scale to emphasise the largest residuals.

Rosenfeld et al. (2013) modelled the emission from the disk around the Herbig Ae star HD 163296 by assuming that the emission arises from an inclined and flared surface with some opening angle, ϕ , relative to the (x, y) plane (the disk midplane), i.e., a ‘double-cone’ morphology. In this way, the front and back sides of the disk with the same projected line-of-sight velocity are spatially offset (see also de Gregorio Monsalvo et al. 2013). Here, a similar toy model is used; however, to determine the line-of-sight velocity, the radius defined in spherical coordinates ($r = \sqrt{x^2 + y^2 + z^2}$) is

adopted rather than that defined in cylindrical coordinates ($\rho = \sqrt{x^2 + y^2}$, as was done in Rosenfeld et al. 2013). For small opening angles the two methods give similar results (the radii differ by no more than 10% for $\phi \leq 25^\circ$). A flared disk with this emission morphology has two possible orientations with either the surface of lower cone or upper cone facing the observer (see e.g., figure 3 in Rosenfeld et al. 2013). Model first moment maps for a flared disk with the same P.A. and inclination as HD 100546, but with three different opening angles, 20°, 45°, and 60°, are shown in Figure A2 in the Appendix.

The range of surface opening angles ([0°, 20°]) is motivated by previous thermo-chemical modelling of CO emission from HD 100546 which suggest an opening angle $\phi \approx 11^\circ$ (Bruderer et al. 2012). The symmetry in the channel maps (Figure 3) also suggests that the emitting layer lies relatively close to the midplane. As before, a coarse grid with a resolution of 5° is initially run over the full parameter space, followed by a zoomed in grid with a resolution of 1°.

Figures 4 and 5 present the statistics and residuals for the best-fit lower cone and upper cone of a flared disk. Using metric (i), the best-fit upper cone model fits the data marginally better (reproducing 65.0% of the velocity field) than both the flat disk and the best-fit lower cone model (62.1% and 62.6%, respectively, see Table 1). The best-fit inclination, P.A., and opening angle are 36°, 145°, and 9°, respectively (see Table 1). The opening angle of the ^{12}CO -emitting surface agrees well with that suggested from thermo-chemical models of HD 100546 (Bruderer et al. 2012).

The best-fit lower cone model has an inclination of 38°, a P.A. of 142°, and an opening angle of 13°. The inclination of this model lies closest to that derived from the continuum observations ($44^\circ \pm 3^\circ$). Despite resulting in a marginally worse fit to the data than the upper cone model (see Table 1), a ‘by-eye’ examination of the residual map (bottom left panel of Figure 5) shows that this morphology best reproduces the velocity field in all quadrants of the outer disk excepting the north-west quadrant for which the magnitude of velocity field is over-estimated. Comparing this residual map to both the channel map (Figure 1) and the eighth moment map (bottom right panel of Figure 3) shows that emission from this quadrant appears less bright and exhibits a positional offset relative to that mirrored across the minor axis of the disk. However, that the upper cone model fits the data best using this metric is in agreement with recent VLT/SHERE images that confirm that the far side of the flared disk surface lies towards the north (Garufi et al. 2016).

For all three models, the global best-fit using metric (ii), i.e., sum of the squares of the residuals normalised by the total number of pixels, is a flat disk with an inclination of 37° and a P.A. of 142°. The best-fit model selected by the smallest peak residual, i.e., metric (iii), is also shared by all three models and is a flat disk with an inclination of 39° (again in good agreement with the other two metrics); however, the disk P.A. which gives the smallest peak residual is 126°. The residual histograms and maps for both of these models are shown in Figure 6. That the inner disk velocity structure is better fit with a shallower P.A. than the outer disk, highlights the presence of a twisted warp: this is investigated in the subsequent section.

Table 1. Best-fit parameters for the flat and flared kinematic models.

Model	Metric of best-fit	Inclination	P.A.	Opening angle	Pixel number	Percentage	Sum of residual squares	Peak residual
Flat	(i)	36°	145°	0°	1590	62.1%	0.737	7.23
	(ii)	37°	142°	0°	1550	60.5%	0.665	6.71
	(iii)	39°	126°	0°	224	8.8%	3.610	3.63
Flared (lower cone)	(i)	38°	142°	13°	1605	62.6%	0.548	6.64
Flared (upper cone)	(i)	36°	145°	9°	1665	65.0%	0.764	7.28

3.3. A warped disk

The residual maps displayed in Figures 5 and 6 reveal two features: (i) a rotating disk within $\approx 1''.0$ of the source position with an inclination angle approximately orthogonal to that of the outer disk, and (ii) a shallower position angle on small scales ($\lesssim 1''.0$) than on larger scales. Both results point towards a twisted warp in the inner disk (see, e.g., Juhász & Facchini 2017, and references therein).

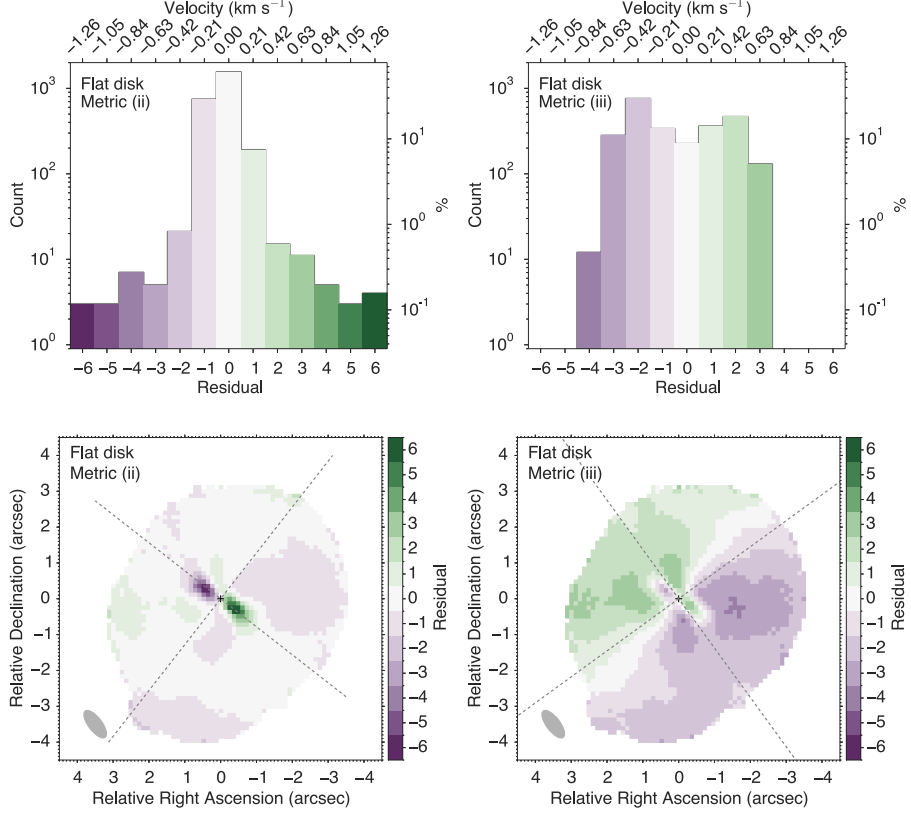


Figure 6. Residual histograms (top) and maps (bottom) for a geometrically flat, rotating disk, using metrics (ii) and (iii) as the measure of best fit. The histograms are displayed on a log scale to emphasise the largest residuals.

Because the residuals are of the order of the size of the synthesised beam, a simple toy prescription for the warp is used. The inner disk is modelled as a planar disk within a fixed radius which possesses its own inclination and P.A., i.e., the inner disk is misaligned relative to the outer disk. This is similar to the approach used by Rosenfeld et al. (2014) to model the kinematics of HD 142527. Figure A3 presents model first moment maps for a warped disk for a range of inclinations and position angles, and for a fixed transition radius of 100 au and outer disk parameters appropriate for the HD 100546 disk.

The outer disk velocity structure is fixed to that of the best-fit upper cone model. As mentioned in the previous section, recent VLT/SPHERE images of scattered light from HD 100546 suggest that the far side of the (flared) disk lies towards the north-east (Garufi et al. 2016). This results in three additional fitting parameters only: the inner disk inclination ($[40^\circ, 90^\circ]$), the inner disk P.A. ($[40^\circ, 100^\circ]$), and a transition radius marking the boundary between the inner and outer disks ($[40, 120]$ au). A coarse grid with a resolution of 10° and 10 au is first run to identify the parameter space containing the global best-fit, followed by a finer grid over this zoomed-in region (with a resolution of 2° and 2 au).

Figures 7 and 8 present the statistics and residuals for the best-fit warped disk, respectively. Metric (i) favours a model with an inner disk that is almost ‘edge-on’ ($i = 80^\circ$) to the line of sight, almost orthogonal to the outer disk major axis (P.A.= 60°), and with a transition radius of 90 au (see Figure 7 and Table 2). These values are consistent with the morphology of the residuals of both the flat and flared models (see Figures 5 and 6). The magnitude of the peak residual of this model is significantly smaller than the previous models selected using metric (i), $4\delta v$ versus $7\delta v$. Metrics (ii) and (iii) select the same model (see Table 2) with parameters similar to those using metric (i); an inclination of 84° , a P.A. of 64° , and a transition radius of 100 au. Comparing the residual histograms and maps for these two models (shown in Figure 8), highlights how a small change in inclination and/or position angle can significantly reduce the magnitude of the peak residual. This latter model results in a peak residual of only $2.4\delta v$ and has the smallest dispersion of residuals: 98% of pixels match the data within ± 0.315 km s⁻¹ and 100% of pixels match within ± 0.525 km s⁻¹.

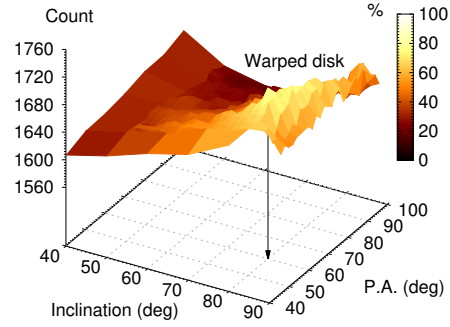


Figure 7. Distribution of model best-fit values using metric (i) as a function of inclination and position angle for the best-fit warped disk. The best-fit transition radius using this metric is 90 au. In this plot, the percentage scale corresponds to the z-axis range.

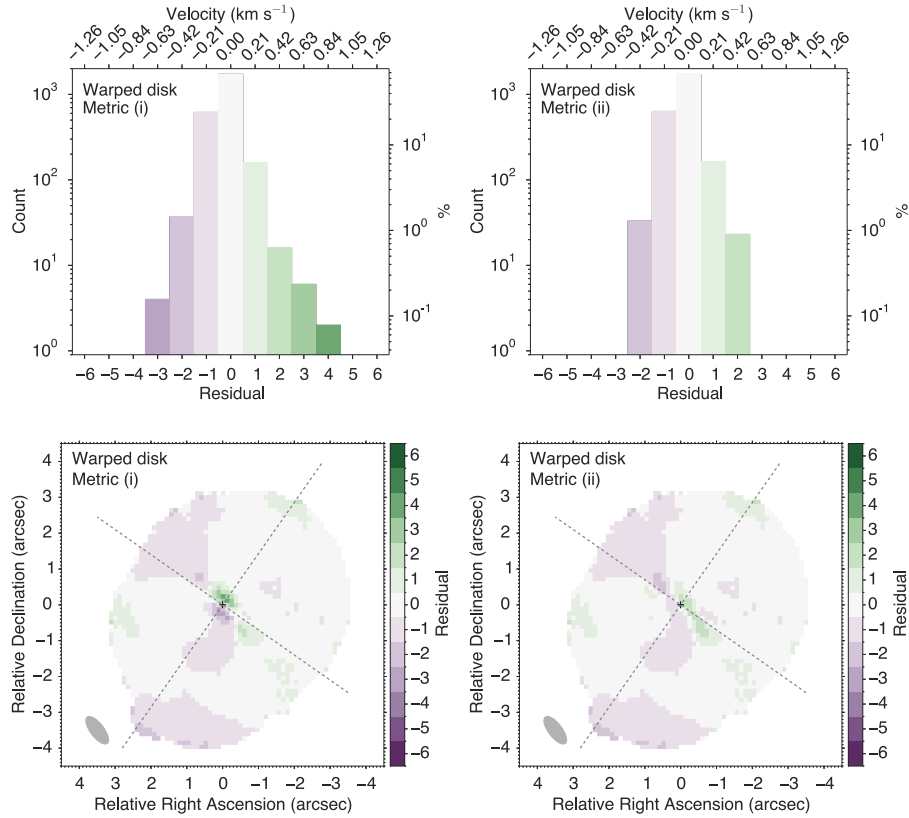


Figure 8. Residual histograms (top) and maps (bottom) for a protoplanetary disk with a warped inner disk using metrics (i) and (ii) as the metric of best fit. The histograms are displayed on a log scale to emphasise the largest residuals. Note that metrics (ii) and (iii) select the same warped inner disk parameters (see Table 2).

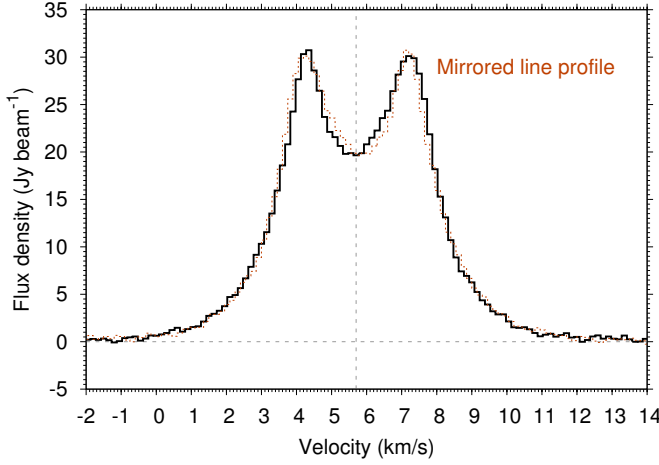


Figure 9. CO $J = 3 - 2$ line profile extracted from within the 3σ contour of the integrated intensity (see Figure 3).

Table 2. Best-fit parameters for the warped kinematic models.

Model	Metric of best-fit	Inclination	P.A.	Transition radius (au)	Pixel number	Percentage	Sum of residual squares	Peak residual
Warped	(i)	80°	60°	90	1722	67.2%	0.387	4.064
	(ii) & (iii)	84°	64°	100	1710	66.4%	0.350	2.441

4. DISCUSSION

The analysis of the kinematics of the HD 100546 protoplanetary disk (traced in ^{12}CO $J = 3 - 2$ emission with ALMA) presented here has revealed the presence of a severely warped (misaligned) inner disk within 100 au of the central star. The inner disk is almost orthogonal to the outer disk and is inclined almost edge-on to the line-of-sight. Figure ?? shows an idealised model of the twisted and warped HD 100546 protoplanetary disk. Higher spatial resolution data are needed to confirm if the proposed warp lies within a smaller radial region than suggested by these data. Scattered light images taken with VLT/SPHERE with a spatial resolution of $0''.02$ reveal no evidence of a severely misaligned dust disk beyond 10 au (Garufi et al. 2016). Hence, if the warp is triggered by the presence of an inner companion in HD 100546, then the warp also lies within 10 au of the central star. Alternatively, the dust disk and gas disk are tracing different physical processes, which is discussed further below.

The presence of a disk warp in HD 100546 was originally proposed by (Panić et al. 2010) and based on asymmetries seen in the red and blue peaks of single-dish spectra observed with APEX. The ALMA data presented here show no such asymmetries in the peaks of the line profile (see Figure 9); however, the mirrored line profile does highlight that the red and blue lobes of emission have different shapes when integrated over the disk. This is consistent with the morphology seen in the channel maps and described in Section 2.

The presence of a warp in the inner disk can shadow the outer disk and lead to an asymmetric temperature structure, because one side of the side is more illuminated by the central star than the opposite side (see figure 3 in Panić et al. 2010). Because the ^{12}CO emission is optically thick, it nicely traces the gas temperature, and thus any perturbations, in the disk atmosphere. Given that the warp is triggered by the presence of a massive companion in orbital motion about the central star, the warp is also expected to orbit with a similar period (as proposed for the case of TW Hya by Debes et al. 2017) and should generate a similar periodicity in the shape of the ^{12}CO line profiles.

The APEX ^{12}CO $J = 3 - 2$ line profile from Panić et al. (2010) shows a stronger blue peak. The dates of the observations taken with APEX and ALMA are November 2008 (Panić et al. 2010) and November 2012 (Walsh et al. 2014), respectively. There also exist multiple APEX observations of the ^{12}CO $J = 6 - 5$ transition. This line profile presented in (Panić et al. 2010) shows an even higher-contrast asymmetry in the blue and red peaks than in the $J = 3 - 2$ line. More recent observations presented in Kama et al. (2016), and taken between April and July

2014, show a similar asymmetry; however, the ratio between the peaks is within the flux density uncertainties of the observations (M. Kama, priv. commun.), so it is currently difficult to draw concrete conclusions on any periodicity in the shapes of the line profiles. A massive ($\approx 10M_J$) planetary companion has been proposed to reside at ≈ 10 au in HD 100546 and that is responsible for clearing the inner cavity in both the dust and gas (Mulders et al. 2013; Panić et al. 2014; Walsh et al. 2014; Pinilla et al. 2015; Wright et al. 2015; Garufi et al. 2016), and dynamical perturbations in [OI], OH, and CO line emission (Acke & van den Ancker 2006; van der Plas et al. 2009; Brittain et al. 2014). A planet at 10 au would have a long period, ≈ 32 years. So if it is this companion that is responsible for the warp, then much longer time baseline observations are needed.

Similar analyses have revealed warps in disks around other stars. Rosenfeld et al. (2012) showed that the kinematic structure of TW Hya could be reproduced using a parametric model of a disk warp with a moderate inclination ($\approx 8^\circ$) at a radius of 5 au. Facchini et al. (2014) demonstrated the observed warp amplitude could be induced by a misaligned close-in companion as massive as $\approx 14M_J$ orbiting within 4 au of the central star. New scattered light data from HST/STIS, coupled with archival data over a 17-year baseline, reveal an orbiting azimuthal brightness asymmetry, with a period of ≈ 16 yr (Debes et al. 2017). The authors argue that this is consistent with partial shadowing of the outer disk by a misaligned inner disk interior to 1 au and that is precessing due to the presence of a $\approx M_J$ -mass planetary companion.

HD 142527 is another protoplanetary disk which has evidence of non-Keplerian motions traced in HCO^+ ($J = 4 - 3$) and ^{12}CO ($J = 6 - 5$) emission (Casassus et al. 2013, 2015). HD 142527 is a transition disk which possesses the largest known dust cavity in sub(mm) emission (≈ 140 au Casassus et al. 2013; Fukagawa et al. 2013). The observed gas motions were postulated to arise from fast (near free-fall) radial flows across the cavity and accreting onto the central star via a severely misaligned inner disk (Casassus et al. 2013, 2015; Marino et al. 2015). Marino et al. (2015) propose that that inner and outer disk are misaligned by 70° . However, Rosenfeld et al. (2014) conducted a theoretical study of fast radial flows in transition disks and showed that the derived velocity profile can also mimic that from an inner disk warp. Better data at higher spatial and spectral resolution are required to determine whether this is an alternative explanation for the inner disk kinematic structure of HD 100546. Indeed, ‘hot-off-the-press’ ALMA observations of HCO^+ ($J = 3 - 2$) line emission from AA Tau at an angular resolution of $0''.2$, also show evidence of an inner warp (or fast radial inflow) in the inner regions revealed by a twist in the first moment map (Loomis et al. 2017).

5. CONCLUSION

The data and analyses shown here demonstrate clearly that the kinematic structure of the disk around HD 100546 cannot be described by a purely Keplerian velocity profile with a global inclination and position angle. Given that there is existing evidence for the presence of (at least) one massive planetary companion orbiting within 10 au of the central star, the presence of a disk warp, albeit with extreme parameters, is currently the most plausible explanation in the absence of any evidence to the contrary. However, the known morphology of the system constrains the radius of the warp to within 10 au meaning that higher spatial resolution data are vital for corroborating the warp hypothesis. Whether the alternative explanation, fast radial flows, could be responsible for the observed kinematic structure of HD 100546 will require higher spatial *and* spectral resolution data, to resolve gas emission across the inner dust cavity ($\lesssim 25$ au), and explore any spatial association with the proposed planetary candidate.

REFERENCES

- Acke, B. & van de Ancker, M. E. 2006, A&A, 449, 267
van den Ancker, M. E., de Winter, D., Tijn A Djie, H. R. E.,
A&A, 330, 145
Andrews, S. M. 2015, PASP, 127, 961
Brittain, S. D., Najita, J. R., & Carr, J. S. 2009, ApJ, 702, 85
Brittain, S. D., Carr, J. S., Najita, J. R., Quanz, S. P., & Meyer,
M. R. ApJ, 791, 136
Bruderer, S., van Dishoeck, E. F., Doty, S. D., & Herczeg, G.
2012, A&A, 541, 91
Bruderer, S. 2013, A&A, 559, A46
Casassus, S., van der Plas, G., Pérez, S. M., et al. 2013, Nature,
493, 191
Casassus, S., Marino, S., Pérez, S., et al. 2015, ApJ, 811, 92
Christiaens, V., Casassus, S., Perez, S., van der Plas, G., &
Ménard, F. 2014, ApJL, 785,L12
Debes, J. H., Poteet, C. A., Jang-Condell, H., et al. 2017, ApJ,
835, 205
Dutrey, A., Semenov, D., Chapillon, E., et al. 2014, in Protostars
and Planets VI, ed. H. Beuther et al. (Tucson, AZ: Univ.
Arizona Press), 317
Espaillat, C., Muzurolle, J., Najita, J., et al. 2014, in Protostars
and Planets VI, ed. H. Beuther et al. (Tucson, AZ: Univ.
Arizona Press), 497
Facchini, S., Ricci, L., & Lodato, G. 2014, MNRAS, 442, 3700
Fukagawa, M., Tsukagoshi, T., Momose, M., et al. 2013, PASJ,
65, L14
Gaia Collaboration et al. 2016a, A&A, 595, A1
Gaia Collaboration et al. 2016b, A&A, 595, A2
Garufi, A., Quanz, S. P., Schmid, H. M., et al. 2016, A&A, 588,

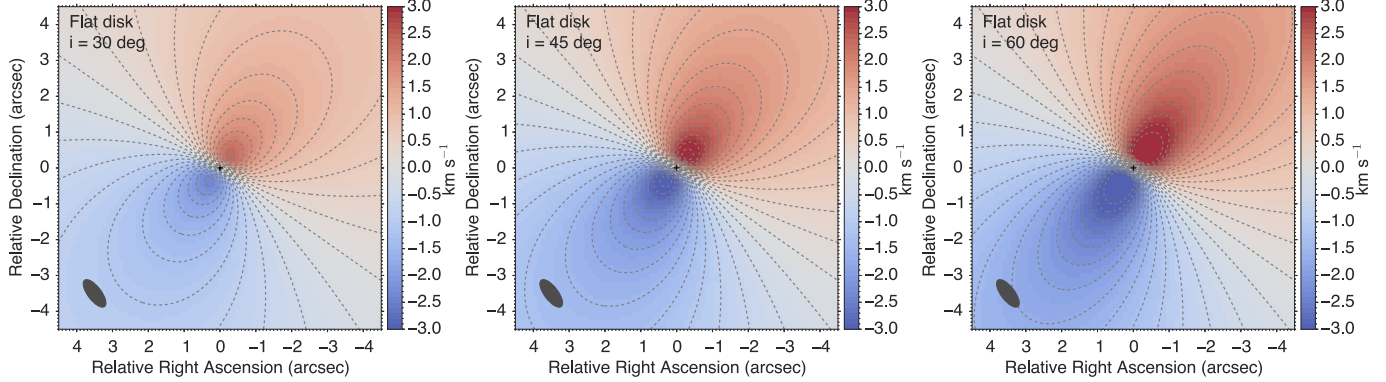


Figure A1. Model first moment maps for a geometrically flat disk with the a P.A. of 145° (representative of the HD 100546 disk) at an inclination of 30° (left), 45° (middle), and 60° (right). The contours are in units of a single spectral resolution element (0.21 km s^{-1}).

- Grady, C., Fukagawa, M., Maruta, Y., et al. 2015, Ap&SS, 355, 253
de Gregorio Monsalvo, I., Ménard, F., Dent, B., et al. 2013, A&A, 557, 133
Juhász, A. & Facchini, S. 2017, MNRAS, in press
Kama, M., Bruderer, S., van Dishoeck, E. F., et al. 2016, A&A, 592, A83
Loomis, R. A., Öberg, K. I., Andrews, S. M., & MacGregor, M. A. 2017, ApJ, in press (arXiv : 1704.02006)
Marino, S., Pérez, S., & Casassus, S. 2015, ApJL, 798, L44
Meeus, G., Waters, L. B. F. M., Bouwman, J., et al. 2001, A&A, 365, 476
Miotello, A., Bruderer, S., & van Dishoeck, E. D. 2014, A&A, 572, A96
Miotello, A., van Dishoeck, E. D., Kama, M., & Bruderer, S. 2016, A&A, 594, A85
Mulders, G. D., Paardekooper, S.-J., Panić, O., et al. 2013, 557, 68
Nomura, H., Tsukagoshi, T., Kawabe, R., et al. 2016, ApJL, 819, L7
Panić, O., van Dishoeck, E. F., Hogerheijde, M., et al. 2010, A&A, 519, 110
Panić, O., Ratzka, Th., Mulders, G. D., et al. 2014, 562, A101
Perez, S., Dunhill, A., Casassus, S., et al. 2015, ApJ, 811, L5
Pineda, J., Quanz, S. P., Meru, F., et al. 2014, ApJL, 788, L34
Pinilla, P., Birnstiel, T., & Walsh, C. 2015, A&A, 580, A105
van der Plas, G., van de Ancker, M. E., Acke, B., et al. 2009, A&A, 500, 1137

- van der Plas, G., Wright, C. M., Ménard, F., et al. 2017, A&A, 597, A32
Quanz, S., Amara, A., Meyer, M. R., Kenworthy, M. A., Kasper, M., & Girard, J. A. 2013, ApJL, 766, L1
Rosenfeld, K. A., Qi, C., Andrews, S. M., et al. 2012, ApJ, 757, 129
Rosenfeld, K. A., Andrews, S. M., Hughes, A. M., Wilner, D. J., & Qi, C. 2012, ApJ, 757, 129
Rosenfeld, K. A., Chiang, E., & Andrews, S. M. 2014, ApJ, 782, 62
Schwarz, K. R., Bergin, E. A., Cleeves, L. I., et al. ApJ, 823, 91
Simon, M., Dutrey, A., & Guilloteau, S. 2000, ApJ, 545, 1034
Semenov, D., Pavlyuchenkov, Ya., Henning, Th., Wolf, S., & Launhardt, R. 2008, ApJL, 673, L195
Tang, Y.-W., Guilloteau, S., Piétu, V., et al. 2012, A&A, 547, A84
Visser, R., van Dishoeck, E. F., & Black, J. H. 2009, A&A, 503, 323
Williams, J. P. & Cieza, L. A. 2011, ARA&A, 49, 67
Walsh, C., Juhász, A., Pinilla, P., et al. 2014, ApJL, 791, L6
Walsh, C., Juhász, A., Meeus, G., et al. 2016, ApJ, 831, 200
Wright, C. M., Maddison, S. T., Wilner, D. J., et al. 2015, MNRAS, 453, 414
Yu, M., Willacy, K., Dodson-Robinson, S. E., Turner, N., & Evans II, N. J. 2016, ApJ, 822, 53
Zhang, K., et al. 2017, Nature Astronomy, in press

APPENDIX

A. MODEL FIRST MOMENT MAPS

Figure A1 shows the first moment maps for a geometrically flat protoplanetary disk for a range of disk inclinations. Figure A2 shows model first moment maps for a flared disk with a fixed inclination for a range opening angles, α , of the emitting surface. Figure A3 shows model first moment maps for a warped inner disk with a fixed transition radius of 100 au, and a range of warp inclinations and position angles. The outer disk parameters are those from the best-fit upper cone model (i.e., an inclination of 36° , a P.A. of 145° , and an opening angle of 9°).

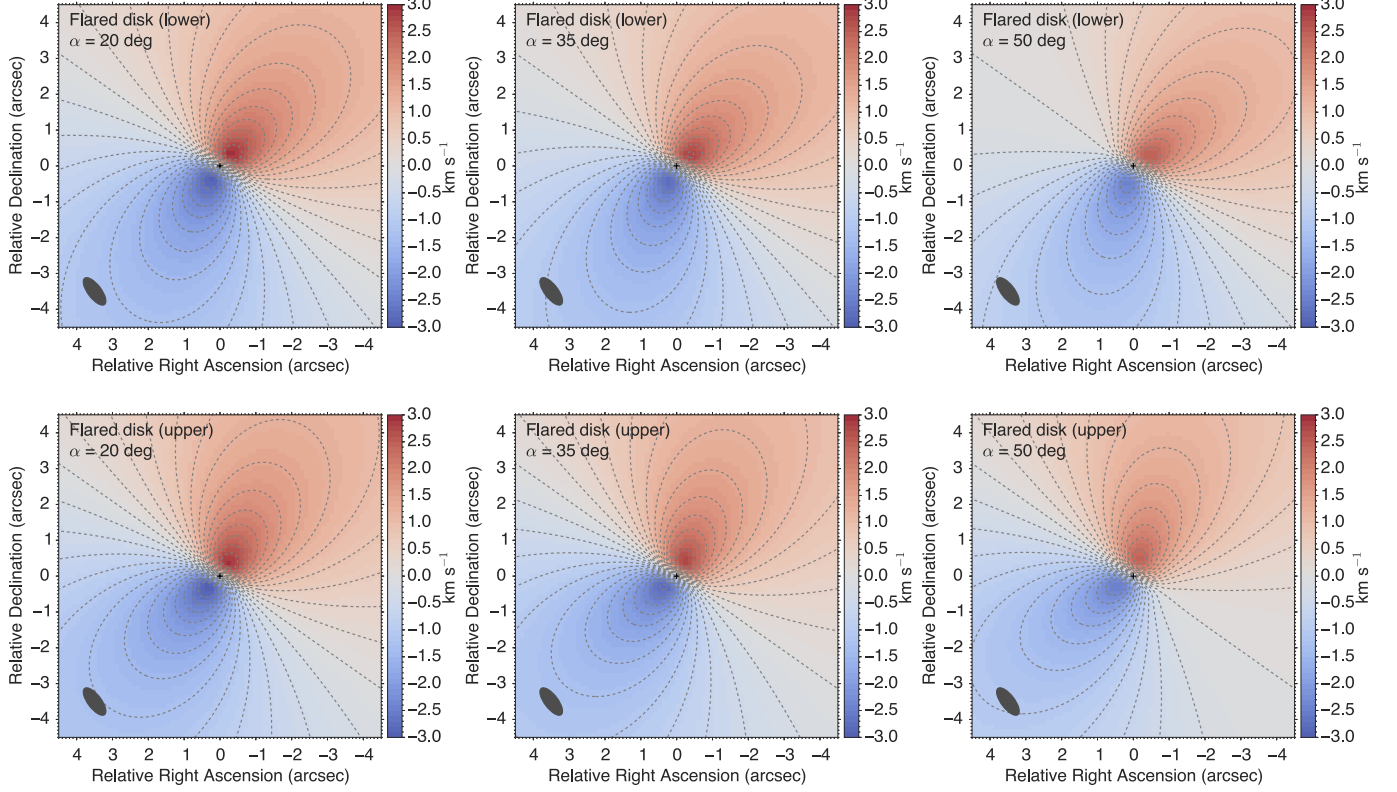


Figure A2. Model first moment maps for a flared disk (lower and upper cones) with a P.A. of 145° and an inclination of 40° (representative of the HD 100546 disk), with an opening angle of 20° (left), 35° (middle), and 50° (right). The contours are in units of a single spectral resolution element (0.21 km s^{-1}).

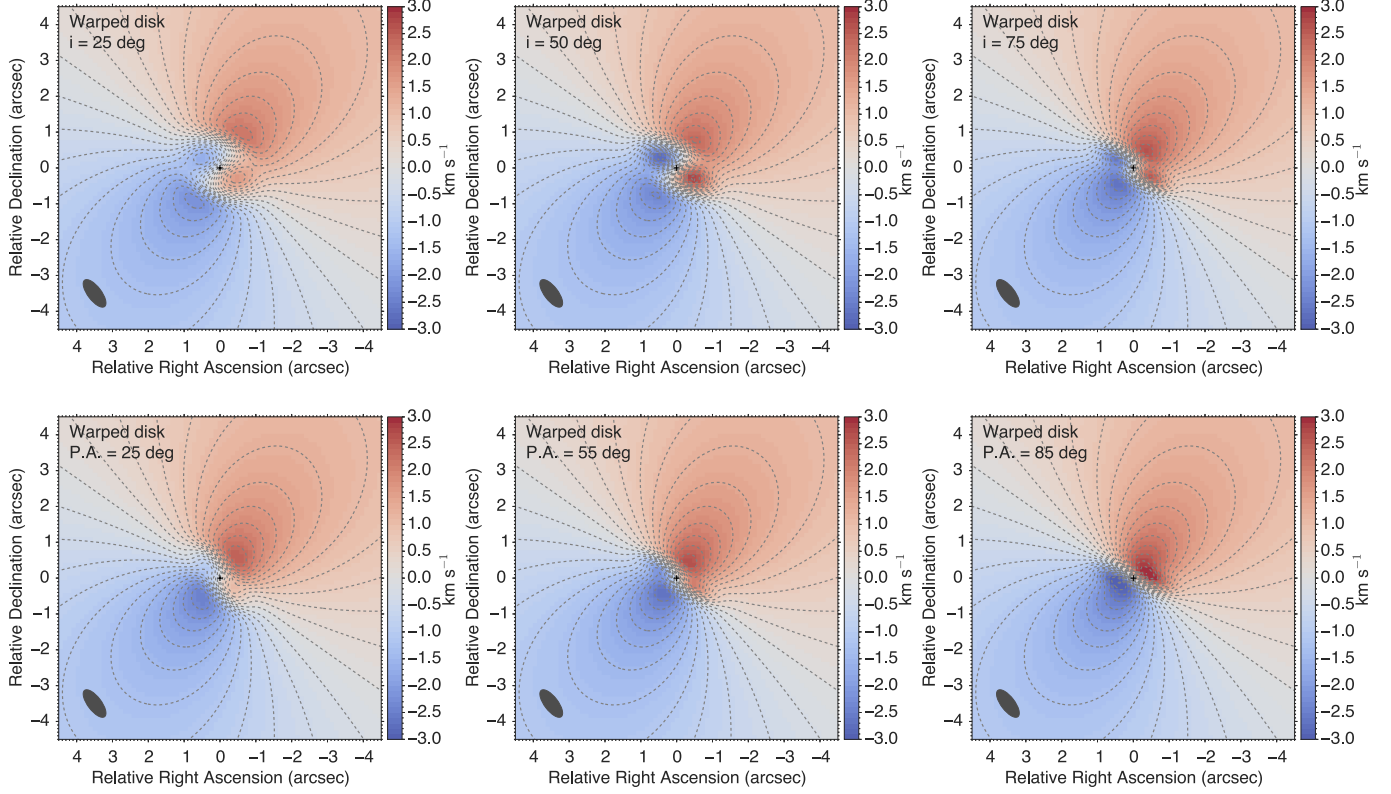


Figure A3. Model first moment maps for a warped disk with an outer disk P.A. of 145° , an inclination of 36° , and an opening angle of 9° . The top row of models have an inner warp with a fixed P.A. of 55° and an inclination of 25° (left), 50° (middle), and 75° (right). The bottom row of models have an inner warp with a fixed inclination of 80° (representative of that in the HD 100546 disk) and a position angle of 25° (left), 55° (middle), and 85° (right). The transition radius in all models is 100 au. The contours are in units of a single spectral resolution element (0.21 km s^{-1}).